

Integrated Photonic FFT for Optical Convolutions towards Efficient and High-Speed Neural Networks

Moustafa Ahmed¹, Yas Al-Hadeethi¹, Ahmed Bakry¹, Hamed Dalir³, Volker J. Sorger^{2,*}

¹*Department of Physics, Faculty of Science, King Abdulaziz University, Jeddah 21589, Saudi Arabia*

²*Department of Electrical and Computer Engineering, George Washington University, Washington, D.C. 20052, USA*

³*Omega Optics, Inc. 8500 Shoal Creek Blvd., Austin, Texas 78757, USA*

**Corresponding author: sorger@gwu.edu*

Abstract

The technologically-relevant task of feature extraction from data performed in deep-learning systems is routinely accomplished as repeated fast Fourier transforms (FFT) electronically in prevalent domain-specific architectures such as in graphics processing units (GPUs). However, electronics systems are limited with respect to power dissipation and delay, both, due to wire-charging challenges related to interconnect capacitance. Here we present a silicon photonics-based architecture for convolutional neural networks that harnesses the phase property of light to perform FFTs efficiently by executing the convolution as a multiplication in the Fourier-domain. The algorithmic executing time is determined by the time-of-flight of the signal through this photonic reconfigurable passive FFT ‘filter’ circuit and is on the order of 10’s of picosecond. A sensitivity analysis shows that this optical processor must be thermally phase stabilized corresponding to a few degrees. Furthermore, we find that for a small sample number, the obtainable number of convolutions per {time-power-chip area} outperforms GPUs by about 2 orders of magnitude. Lastly, we show that, conceptually, the optical FFT and convolution-processing performance is indeed directly linked to optoelectronic device-level, and improvements in plasmonics, metamaterials or nanophotonics are fueling next generation densely interconnected intelligent photonic circuits with relevance for edge-computing 5G networks.

1. Introduction

With an ongoing trend in signal processing and computing towards higher degrees of system heterogeneity, specialized and domain-specific processors are gaining interest [1]. In this context, the rise of emerging neuromorphic platforms for artificial intelligence (AI) acceleration include optical [2-5] and photonics neural networks (NN) [6-8], which also contain emerging plasmonic and meta-materials for both the dot-product linear synaptic weights, and the nonlinear activation function [9,10]. Photonic or electro-optic concept for the neuron implementation include, amongst others, electro-optic analog weighting [8-10] and spiking-based solutions e.g. Ref [6]. For the neuron interconnectivity the broadcast and weight protocol use wavelength-division-multiplexing (WDM) to assign a dedicated optical wavelength to each neuron, and multiplexes all signals onto a common photonic bus, thus enabling fully-connected NN [6-8] or all-optical [12]. The second popular choice relies on a phase-sensitive linear network of cascaded MZI performing a unitary matrix multiplication, see for example Refs. [8, 13].

A third option borrows inspiration from Fourier optics, namely a 4F Fourier optical system [2]; to gauge the possible performance potential of such as system, let us consider a lens with focal length of 15 mm and 15 mm diameter which has an optical latency of 0.16 ns on the marginal ray and at 1550 nm, 46.8 million diffraction limited pixels enable a throughput of 300 petahertz. If each pixel is modulated with 8 bits, this results in 2.4 exabits/s of signal processing in a volume of 5.3cm³ [4]. Naturally, this is an upper limit of what may be physically possible and engineering challenges will place a much lower realistic bound, nonetheless it stands to reason, that Fourier-optics based accelerators bear much potential for in signal processing and special purpose processors to perform correlations and convolutions as a fundamental building block. While free-space 4F systems are capable of high parallelism such as by utilizing digital light processing (DLP) technology [3-5, 14], they are limited with respect to a) delay given the often meter-scale

setups, b) hence large and bulky footprints, and c) slow update rates from modulating elements such as spatial light modulators (SLM) which only clock at about 60 Hz, e.g. Ref [15]. Thus, the rationale is to combine Fourier-optics based signal processing with integrated photonics capabilities, which thus enables a) fast update rates of state-of-the-art integrated photonics such as modulators, phase shifters, and photodetectors delivering a foundry-ready capability of 10's of GHz speeds, hence a speed up of about $10_{10}/10_2 = 8$ orders of magnitude, and b) significantly increased form-factors of square millimeters (for the active chip at least) rather than 0.1-1 square meter of free-space 4f systems. However, the shortcoming to an integrated photonics-based Fourier filter is to trade-off parallelism as further discussed below. Hence, naturally those applications that require a short delay inference and low computational footprint such as network-edge processing benefit most from an integrated FFT-based optical processor. The rationale for this paper is to explore the performance of an integrated photonics Fast Fourier transform (FFT)-based processor. We first introduce two alternative concepts of a parallel and a serial processor, and thence analyze its performance with respect to phase and temperature sensitivity before concluding with a size-scaling performance comparison against a GPU.

2. System Architecture, Design and Operation

A unique feature of an electromagnetic wave is its ability to execute the mathematical operation of both addition and subtraction as it propagates. Such wave interference-based arithmetic forms the basis of several optical effects and system to include, but not limited to, holography, phased array antennas, and interferometric microscopy. Notably, these systems are energy-wise 'passive' or reprogrammable filters, with the only energy consumed by these arithmetic operations in case when losses are incurred of the traversing optical beam or signal. Incidentally, frequency domain filtering is a technique that is deployed since the middle of the last century with Fourier optics. In such an optical processor, a Fourier lens performs an FFT by converting the signal (e.g. an image, RF data, ...) into the frequency domain where filtering can occur. The so-filtered and hence processed signal is thence being converted back into the spatial domain with a second lens, i.e. inverse FFT (IFFT). Indeed, executed in free-space operating on the full image such as 1000x1000 pixels, namely one million parallel channels, these systems are highly parallel but also bulky, as mentioned above. Conceptually, the rationale to utilize optical interference for the FFT portion was first introduced by Marhic [16]. Indeed, originally a star coupler is used to perform addition and subtraction and length differences are used to rotate phase. Advances in on-chip photonics as well as simplifications of the waveguide layout [17-19] have led to realizable optical OFFTs in silicon-on-insulator (SOI) technology. While the most immediate application for the OFFT is in high bandwidth communications where frequency domain representation can break a large bandwidth into many sub-bands for orthogonal frequency division multiplexing (OFDM), a more recent application for frequency domain representation is found in convolutional neural networks (CNN). CNNs performing the crucial function of feature-extraction in machine learning applications; speeding up this computationally heavy part in machine learning is one of the principal rationales for the work presented herein.

A CNN is a neural network where instead of fully connecting each input to each output with weights, convolutional filtering connects the network in a spatially local manner [20]. This convolutional filtering is normally performed by GPUs, which convert the input data to the frequency domain with a forward FFT where it is multiplied by a kernel and then converted back into the spatial domain with an IFFT. By using an OFFTs for convolution instead of GPUs, a system can be built to take advantage of the energy efficient arithmetic of wave interference to perform the convolutions of the CNN (**Fig. 1**). Here the CNN is comprised of FFT point-wise dot product multiplication in the Fourier domain (i.e. frequency filtering), and inverse OFFT. The challenge of this system is that it requires phase coherence, a sensitivity analysis is discussed below. The OFFT is built on three passive components: the two-by-two coupler is used for addition and subtraction, waveguides with short path differences are used for phase rotation, and waveguides with long path differences are used for signal delay [19, 20]. While in principal an OFFT network could be created with perfect phase alignment at a specific temperature, in practice active phase calibration is required to compensate for fabrication and temperature variance. This phase calibration is normally accomplished with heating elements placed along one of the waveguide paths of each waveguide pair. The Cooley-Tukey FFT requires two operations: addition and multiplication by a phase. The two-by-two optical coupler forms the principal addition equation of the OFFT, Eq. 1.

$$\beta_1 = \frac{1}{\sqrt{2}}(-\alpha_1 + \alpha_2)$$

$$\beta_2 = \frac{1}{\sqrt{2}}(\alpha_1 + \alpha_2) \quad (1)$$

where β_1 and β_2 are the outputs and α_1 and α_2 are the outputs of the 2×2 coupler. The phase multiplication required by the Cooley-Tukey FFT can be implemented optically by phase difference, Eq. 2.

$$\epsilon_{xy} = \exp(-i2\pi xy/N) \quad (2)$$

With these two components, the butterfly pattern (**Fig. 1b**, inset) of the Cooley-Tukey FFT can be built using only passive optics (omitting phase control). Unlike OFDM, convolution works with spatial data and hence requires a two-dimensional (2D) FFT. The $M \times N$ 2D FFT can be composed from row and column operations of M length N FFTs plus N length M FFTs. For a square matrix this becomes $2N$ FFTs of length N each. In the OFFT there is a choice between implementing a large 2D FFT network directly or implementing a smaller 1D FFT in the complex domain and using it repeatedly in time for each row and column operation [21]. While complex OFFTs have not been directly discussed in the literature, Eq. 1 and Eq. 2 hold for complex signals. To generate a complex OFFT an additional reference signal path must be mixed with the output prior to digitization to determine both phase and amplitude, like an optical heterodyne Quadrature Phased Shift Keying (QPSK) receiver. Otherwise, phase can be measured by phase-difference as in an optical Differential Phased Shift Keying (DPSK) receiver. In the phase-difference method, two cycles of the OFFT are required however; the first cycle sends a known signal through the OFFT circuit and measures the real and imaginary part at the output; the second cycle then sends the actual signal through the network and again measures the both complex parts of the signal relative to the calibration signal. In either the heterodyne or the differential case, the complex and real measurements can be split into two separate cycles of the OFFT to save use of ADCs. In the two-cycle approach, the unmodified signal is fed through the OFFT and the real part of the output is measured. Next, the signal multiplied by i (imaginary number), is fed through the OFFT and the real part is measured. The first cycle then measures the real part of the result and the second measures the complex part.

Knowing both the real and imaginary part of the FFT at the output allows the OFFT to be reused across several cycles to create the 2D FFT required for the CNN. Additionally, the 1D Cooley-Tukey algorithm can be divided over multiple cycles due to its recursive nature, which allows scaling down the size of the OFFT properly for the application in use, with a tradeoff between the number of ADCs and DACs and their operating speeds. Indeed, many ADCs and DACs can be replaced by a smaller number operating at a higher speed. Allocating delay presents another design decision. Overall, the architecture can be serial, with a single sampling modulator (**Fig. 2a**) and optical delay, or alternatively parallel with N sampling modulators (**Fig. 2b**). Whereas the serial case requires less power, with only one DAC, it also has a lower convolution rate, since only one convolution result can be realized within the period of the longest delay path.

3. Results and Discussion

Next we discuss the sensitivity of the performance of the OFFT exemplarily on a $N=4$ FFT and extrapolate the performance of a CNN based on a 2D OFFT including performance as a function of N scaling (**Fig. 3a**). Interestingly, the FFT delay decreases linearly with increasing modulation rate, a distinctive feature of optics. The on-chip portion of the OFFT consists of cascaded delayed interferometers and passive components such as directional couplers, y branches, straight and spiral waveguides, and operates on time domain signals (**Fig. 1**). We opted for a SOI platform as a cost-effective platform and reliable fabrication process [22]. The length of the OFFT MZI phase shifter is determined by the system frequency (i.e. signal modulation), $f_s = 10 \text{ GHz}$, then the required time delay becomes $T_{Delay} = \frac{1}{f_s}$ and the physical length, $d_{10} = (c/n)T_{delay} = 12 \text{ mm}$, hence the MZIs in the waveguide lengths for the delays are trivially computed to be $T/2$ ($T/4$) = 3 (6) mm. The stage-1 MZI must compensate for phase shifts created by fabrication and temperature variances; the relative phase tuning range should cover $\pi/2$ requiring thermal control: with $\frac{dn_{eff}}{dT} \approx \frac{dn}{dT}$ and Silicon's thermo-optical coefficient ($\frac{dn}{dT} = 1.9 \times 10^{-4} \text{ K}^{-1}$), the phase change is given by:

$$\Delta\phi = \frac{\pi}{2} = \frac{2\pi}{\lambda} \frac{dn}{dT} \Delta TL. \quad (3)$$

For the stage-2 ($N=4$) MZIs the temperature change required is 4.2 K, thus, temperature control must not be ignored, and hence we integrate resistive heaters on one of the MZI arms to tune the desired refractive index change. We

selected a minimum waveguide bending radius of $50 \mu\text{m}$ to keep the radiative bending losses low, resulting in a delay-line spiral area of $3.9 \times 10^{-3} \text{ mm}^2$ for T . Sampling is required to obtain the frequency components of the transfer function of the FFT, realized with back-end electro-optic modulators (EOM) in silicon photonics e.g. Ref [8] or alternatively with emerging modulator-concepts featuring heterogeneous integration of strong-index changes materials such as transparent conductive oxides featuring strong light matter interaction near epsilon near zero (ENZ) operating points [23,24], and micrometer compact MZI ITO-based modulators [25-27], see also work from the Wong and Brongersma groups (see **Fig. 4** for nanophotonics-enabled OFFT and convolution performance outlook). Selecting the SOI modulators for now results in a total OFFT area to about 0.019 mm^2 ($N = 4$). The OFFT design allows placing the EOMs either before or after the FFT butterflies. However, in order to minimize detuning phase, delay, and optical loss differences across the four modulators, the EOMs can appear at the end of the last stage of OFFT to ensure synchronous sampling (**Fig. 3b,c**). To avoid power mismatch loss from the difference in waveguide length of the cascaded MZIs, ‘waivy’ waveguide bends are added to the shorter arm of the interferometers to compensate for the power loss at the output of the couplers and are executed with a Python script feeding into a CAD-tool for photonic waveguide placement.

Next we analyse the sensitivity of the OFFT transfer function; conceptually the FFT separates frequency contributions of the temporal input signal. Since the system frequency is 10 GHz, the frequency spacing of the OFFT output channels match this closely, but the exact location of the probe frequency for which the maximum transmission is obtained for different outputs is a function of time delay and can vary across the outputs. This will create a variation in every four transmission peaks at a specific frequency the contributions from the neighboring channels ($X_i = \text{OFFT output channel number}$, $i = 1-4$ for $N = 4$, **Fig. 3d**). Analyzing this transfer function and the extinction ratio of the cascaded interferometers, the discrete nature of the OFFT yields intrinsic quantization errors in frequency and sampling artifacts that are a function of the phase. We analyze the phase- and time delay, and optical loss in particular that of the lower arm of the interferometer in the first stage of the OFFT (**Fig. 3d,e**), and evaluate the change in the transfer functions of the output. This location is particularly impactful on the transfer function, since it has the highest oscillation and narrow spacing in the frequency domain [29]. Our observable is the frequency detuning of the maximum point of the transfer function, which, for instance, for output port X_2 appears near 6.8 GHz (**Fig. 3d**). At the ideal case for vanishing phase detuning, the entire power exits at the second branch X_2 of the top interferometer due to the additional phase, i.e. the relative phase difference in bidirectional coupler, where it is sampled by a modulator.

With phase detuning away from the ideal design point, however, the energy of the output transfer functions can leak to the neighboring ports (**Fig. 3e**); for instance, the power of the first interferometer shifts to the top of the second stage lower interferometer exiting of at the next frequency probe (16.78 GHz), since each output bin in the frequency domain has a 10 GHz spacing, determined by the chosen system frequency. By sweeping the frequency, we can find points at which the OFFT has the highest transmission, defined by time delay. Hence the effective impact of the phase detuning is a lateral frequency shift. In the ideal case of no phase variation and at different probe frequencies (frequency at which each OFFT output has a maximum transmission in power), full transmission can be achieved. However, deviations in phase change the output amplitudes respectively where the maximum transmission decreases until it vanishes, while the next full transmission from another output port becomes dominant, which occurs as a cyclic behavior. Note, that the value of 6.78 GHz is not significant by itself, as it can be shifted by detuning the delay lines. However, to determine the overall quality of this cascaded system of interferometers, we set a threshold for the phase-detuned power ratio (i.e. frequency power leakage) between target-to-neighboring output ports; here we select a -20 dB channel-to-channel separation threshold, which is typical for telecommunication applications [29]. Given this threshold, the maximum phase tolerance is < 0.2 radians to ensure acceptable spectral leakage, i.e. channel crosstalk (**Fig. 3f**). Physically this range corresponds to a small ($\Delta T = 0.54 \text{ K}$) temperature change that the waveguide index must tolerate to keep within the selected attenuation threshold, consequently demanding phase control. One potential approach is to place the OFFT chip in an ambient chamber with temperature isolation such that the heat could be transported to only the specific areas as desired. Alternatively, control loops and temperature stabilization of the chip could also be employed. Indeed, we observe a nonlinear phase error, which is likely due to nature of cascaded interferometers and their phase sensitivity with respect to physical delay lines. To probe the effects of phase detuning errors and distortions in the signal further, we study the difference in the transmission power ($P_{\text{degradation}}$) as a function of phase (**Fig. 3f,g**). Thus, the signal-to-noise ratio $SNR = \frac{(P_{\text{out}} - P_{\text{degradation}})}{P_{\text{degradation}}}$ is obtained by taking the difference in the transmission output power values relative to the ideal zero phase, and, thus, determines the performance quality of the OFFT in response to optical phase noise. We define the power mismatch ratio and FFT quality (i.e. figure of merit, FOM) as follows:

$$P_{mismatchRatio} = \frac{P_{out1}}{P_{out2}}(\phi) \quad (4)$$

$$FOM = \frac{SNR}{P_{mismatchRatio}} \quad (5)$$

The idea behind the definition is that the smaller the power mismatch ratio (deviation from unity), and the higher the SNR in the system, the higher the quality of the OFFT as a function of detuning phase. As a result, the system performs best at the ideal zero phase case as expected for X_2 since the power mismatch ratio between X_2 and X_0 is close to 1, where FOM is maximized. For the case of X_1 and X_3 however, their SNR values are low, despite the power mismatch ratio being close to unity 1, since their transmission is minimal for frequency contribution at 6.78 GHz. The maximum FOM for all four outputs aligns with the design probe frequency value for each frequency bin. As the phase is swept the FOM also decreases drastically for X_2 and even further for X_3 since the OFFT output detunes away from the probe frequency (max. transmission), as a result SNR decreases.

For ideal OFFT filtering and optimal transmission, the output power of the cascaded MZI arms must match. This, however, is challenging since in the OFFT design the MZI arms have different physical lengths, hence, in order to understand how the difference in length changes the quality of the OFFT output, the MZI extinction ratio (ER) was analyzed by sweeping the delay and additional loss in the first and correspondingly second stage of OFFT (Fig. 3h,i). The extinction ratio is defined as $ER = \frac{P_{max}}{P_{min}}(\gamma_{loss})$ where P_{max} (P_{min}) is the maximum (minimum) power at the output of the OFFT, and the delay lines corresponding to loss values were altered across the lower arm of the cascaded MZIs. Note, that in the second stage the delay is half of the first stage, and so is the loss. This is important for consistency and symmetric operation in the overall system design. As proven analytically by the ideal coupler's extinction ratio behavior in the lower arm (Fig. 3i), the loss increases exponential with waveguide length as expected. However, the loss increases if the length imbalance increases. This is because of the extra power mismatch between the MZI arms, impacting the quality of the OFFT's transfer function. Thus, the aim is to maximize ER similar to modulators [25-28] and 2x2 direction coupler electro-optic switches e.g. a $< 10 \mu\text{m}$ compact option is Ref [30], but with the difference of improving the power mismatch between the MZI arms rather signal device on-off ratio. Another significant scaling factor in the OFFT resides in increasing the optical losses from a growing the number of branches and waveguide delay lengths at high N . The optical power at each output must be sufficiently high to meet the noise requirements for the number of bits at the detector. With the total loss for a single output being the sum of the losses in dB at each $\log_2 N$ stage, in the serial architecture, the longest arm of a stage passes through a 3-dB branch and a MZI-spiral with a length that scales with N . At high N the loss becomes dominated by the $N \log_2 N$ scaling of the spirals.

4. Performance: sample scaling, power and speed

The OFFT in silicon photonics becomes a network of delay waveguides, Y-branches, Mach Zehnder Interferometers (MZIs), and heater-calibrated phase delay waveguide segments (Fig. 3a-c). In the serial case (Fig. 2a), delay is implemented with spiral delay stages. The spirals scale in area proportional to their length. The length of the first spiral is the greatest and they diminish in length with $(1/2)^k$, where k is the stage index. There are $\log_2(N)$ delay stages each with 2^k spirals. Even though the number of spirals doubles with each stage, the area stays constant due to the spiral length halving with each stage. Thus, the area relative to the first spiral scales with $\log_2(N)$ and the first spiral with scales with N for a total area scaling of $N \log_2(N)$.

It is apparent that due to the passive nature of the OFFT network, the primary power consumer in the small- N OFFT is found in the conversion between the digital and analog domains. If the OFFT were directly connected to an analog fully connected neural network or some other analog processor, the only power consumed by the OFFT would come from optical propagation losses, phase compensation, and the coherent optical source. However, today's dominant computer architecture is digital, and to be practical, the OFFT implementation must interface to the digital domain. The power consumption analysis becomes an analysis of digital and analog conversions. Recent developments in DAC and ADC designs now also allow leaving the signal in the optical domain altogether (no O-E-O conversion required), thus reducing system design complexity [31].

The FFT data capacity, the number of bits that can be propagated through the system, depends on the modulation type; assuming QAM 256 for a high SNR channel with a bandwidth of 10 GHz the upper bound for bandwidth is 80

Gbps for a single OFFT channel and 320 Gbps for $N = 4$. While we have analyzed the sensitivity and performance for $N = 4$, it is interesting to ask how larger systems scale. Increasing the number of FFT-samples (N), our OFFT grows with $(N - 1)$ cascaded delayed interferometers and $2(N - 1)$ couplers. Unlike an electronic FFT however, which scales with approximately $5N \log_2 N$, the optical FFT will need to compensate for increasing optical losses with greater optical power. Our FFT scaling analysis shows performance peaks for the OFFT for small N , which outperforms an electronic (NVIDIA P100 GPU) for $N < 200$ (**Fig. 4**) [32]. The results of the performance-scaling characteristics of the OFFT using the highest speed DAC and ADC found in literature today, and comparing against NVIDIA P100 GPU, shows up to 20 times improved performance even with the high power consumed by the converters. The NVIDIA P100 performs 1.6 TFLOPS during single precision 1024 length FFT [32]. Assuming the 1D FFT requires $2N \log_2(N)$ multiplication operations and $3N \log_2(N)$ addition operations there will be a total of $5N \log_2(N)$ FLOPS per 1D FFT of length N . To generate a 2D FFT with an edge length of N from a 1D FFT there will be $2N$ 1D FFTs of length N for each 2D FFT. To complete the convolution there will be one N^2 multiply in the frequency domain and one inverse 2D FFT to return to the spatial domain. Then the number of FLOPS to convolutions becomes $20N^2 \log_2(N) + N^2$. With the GPU from above this results in a convolution rate of 7 KHz with $N = 1024$ and 150 KHz with $N = 256$. Modern DAC operate at about 100 GSa/s and consumes 2.5 W [33], while ADCs show 56 GSa/s consuming 2 W per channel [34]. Assuming integrated germanium photodetectors [35] with a reverse bias of 8 V and 250 μ W of optical power, the power consumption in each photodiode is approximated as 2.4 μ W. Using these assumptions, we model both serial and parallel implementations of the OFFT convolutional architecture and compared them to the NVIDIA P100 GPU using a 2D OFFT convolutional filter (1-stage of a CNN) system performance FoM defined as number of convolutions $s^{-1} W^{-1} m^{-2}$ (**Fig. 4**). Note, this system FoM is different from the OFFT sensitivity FOM discussed in Eq. 5 above. The results of the analysis show that with a small convolution size the photonic approach is outperforms electronics (e.g. P100 GPU) (**Fig. 4**). However, the advantage diminishes as the convolution scales, which is due to the approximate scaling of the FoM with $1/(N^4 \log_2 N 10^{(N \log_2 N)/10})$ in the serial photonic case, $1/(N^4 \log_2 N)$, in the parallel photonic case, and $1/(N^2 \log_2 N)$ in the electronic case. The contribution to the serial photonic FFT scaling are from $1/(N \log_2 N)$ in area, $1/(10^{(N \log_2 N)/10})$ in optical power, $1/N$ in ADC power, $1/N^2$ in samples to area. Shortly beyond $N = 102$ the power efficiency of the P100 overtakes the serial photonic approach and near $N = 104$ the P100 passes the parallel OFFT architecture. This model assumes a constant TFLOPS performance for the P100 independent of N . A more realistic model would reduce the TFLOPS performance of the GPU at higher N due to pipelining and memory bandwidth limits. While these encouraging initial results, further improvements are anticipated as optoelectronic components evolve including nanophotonics, plasmonics or metamaterial-based principles to deliver <1fJ/bit level devices [36]. If such level of efficiency was achievable, the photodiode and electronic ADC in our previous analysis could potentially be replaced with a set of 256 single bit receivers operating at 10^7 's of femtojoules per bit. In this case, the power at each 8 bit 56 GSa/s receiver could be reduced to as little as 5 mW.

5. Conclusion

In conclusion, we explored the design and operation sensitivity of a temporal $N = 4$ photonic integrated circuit-based fast Fourier transform (FFT) nanophotonic paradigm. Our design based on cascaded interferometers shows both phase and time delay (loss) sensitivity. We obtain the transfer function of this photonic function by monitoring the frequency bins at the output ports of the FFT sampled by electro-optic modulators. A sensitivity analysis shows that the thermal operating range is achievable, yet somewhat narrow, in order to adhere to telecommunication-relevant phase thresholds. Control over this range, however, is possible with thermal on-chip heaters on the MZI arms of the silicon waveguide sections. Unlike electronics, here the number of FFT data processed per second only depends on the time-of-flight of a photon through the millimeter short photonic chip. As such, we find the performance (number of FFTs or convolutions performed data per second, power, and areal footprint) outperforms state-of-the-art graphical processing units (GPUs) by 2-3 orders of magnitude for a low number of convolutions. Nanophotonics component level developments of modulators and directional coupler switches, for instance, can enable even higher performance enabled by a more efficient way of engineering strong light-matter-interactions [25-28], which can incidentally also be used to engineer the nonlinear activation function [37] for a variety of photonic neural networks. Taken together this temporal FFT shows how photonics enables data processing by simple routing light for an in-the-network-computing [4], photonic domain-specific engines such as CNNs e.g. Ref [11] rather than using photons for classical transceiver communication in networks or network-on-chips [39].

Figure 1

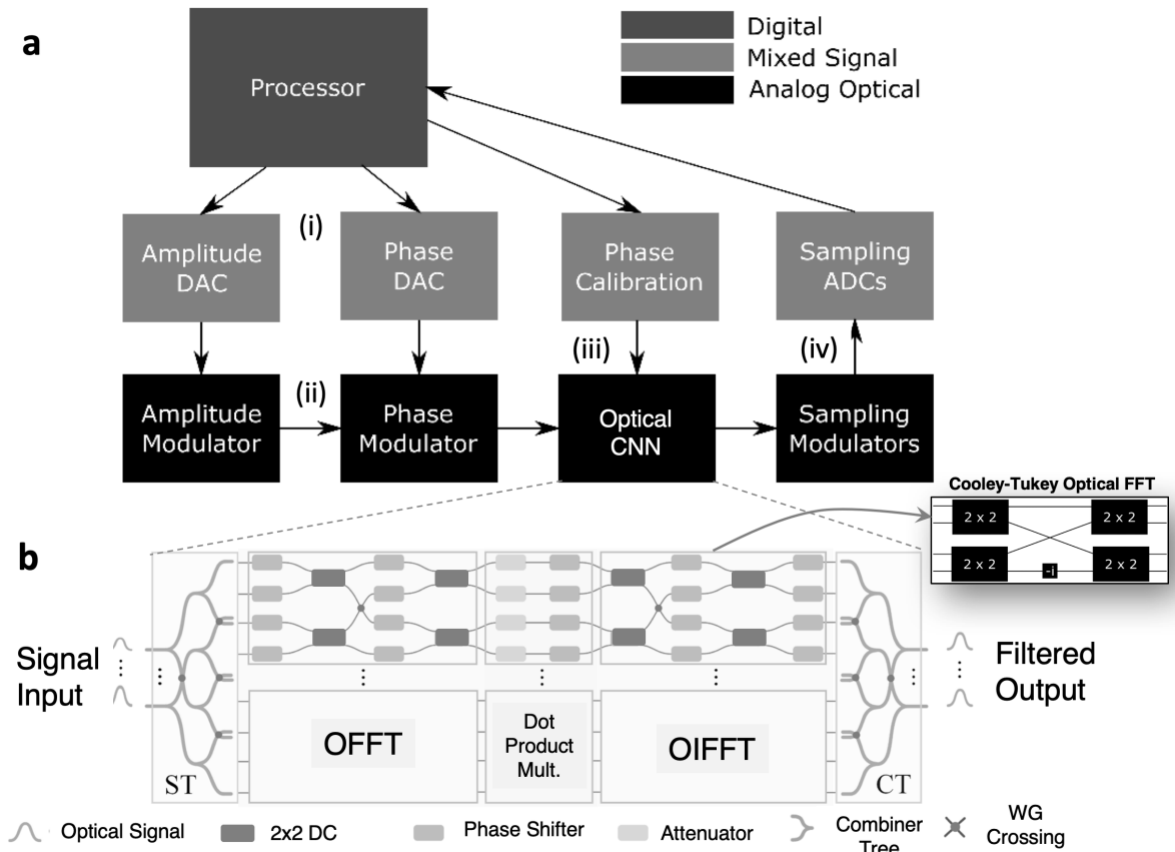


Figure 1. Photonic CNN paradigm utilizing Fourier-optics based on integrated photonics. a, Block diagram of the photonic processor utilizing optical FFT to perform convolutions showing the data flow from the processor to the amplitude and phase Digital to Analog Converters (DACs) (i), being modulated onto an optical carrier (ii) flowing through the phase calibrated OFFT network (iii) and being converted back into the digital domain (iv) with sampling Analog to Digital Converters (ADCs) and optional sampling modulators. **b**, Layout of photonic (on-chip) FFT and element-wise dot-product multiplication. Coherent components: ST = waveguide splitter, CT = waveguide combiner, including waveguide crossings. Details of the OFFT rely on an optical Cooley-Tukey FFT as discuss next. Inset: The 4 x 4 butterfly pattern of the Cooley-Tukey OFFT is composed of a set of passive optical on-chip components in SOI technology. 2 x 2 optical couplers provide addition and subtraction while a small path-length difference in one of the waveguide branches provides the reciprocal root-of-unity change in phase.

Figure 2

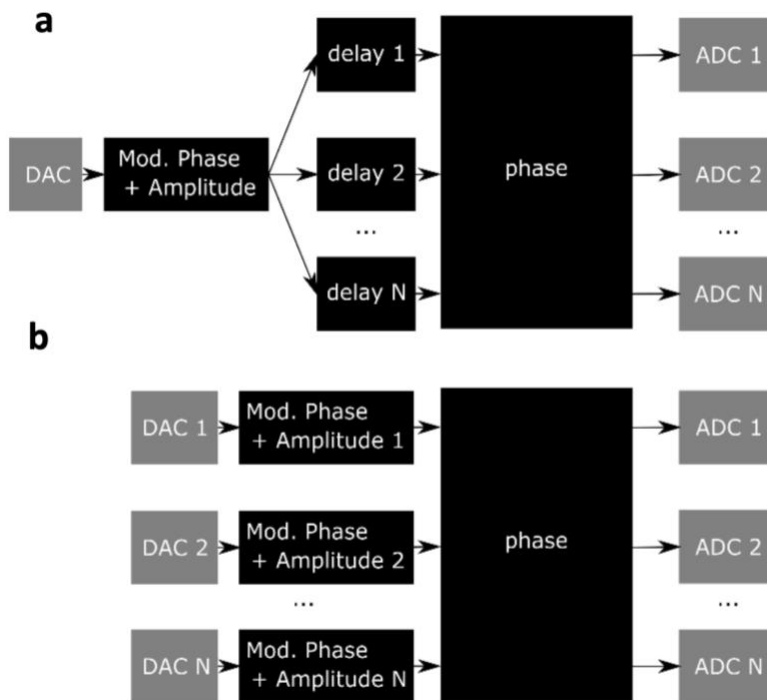


Figure 2. Two Options of implementing the OFFT. **a**, The optical convolution can be run in serial with a single digital-analog-converter (DAC) and optical delay in the photonic network, or **b**, with N parallel DACs and no additional delay in the photonic network. ADC = analog-digital-converter. Seamless all-photonics DACs could enable reduced OFFT and CNN design complexity, thus enabling higher scaling potential while reducing power consumption due to eliminating the parasitic O-E-O conversion [38].

Figure 3

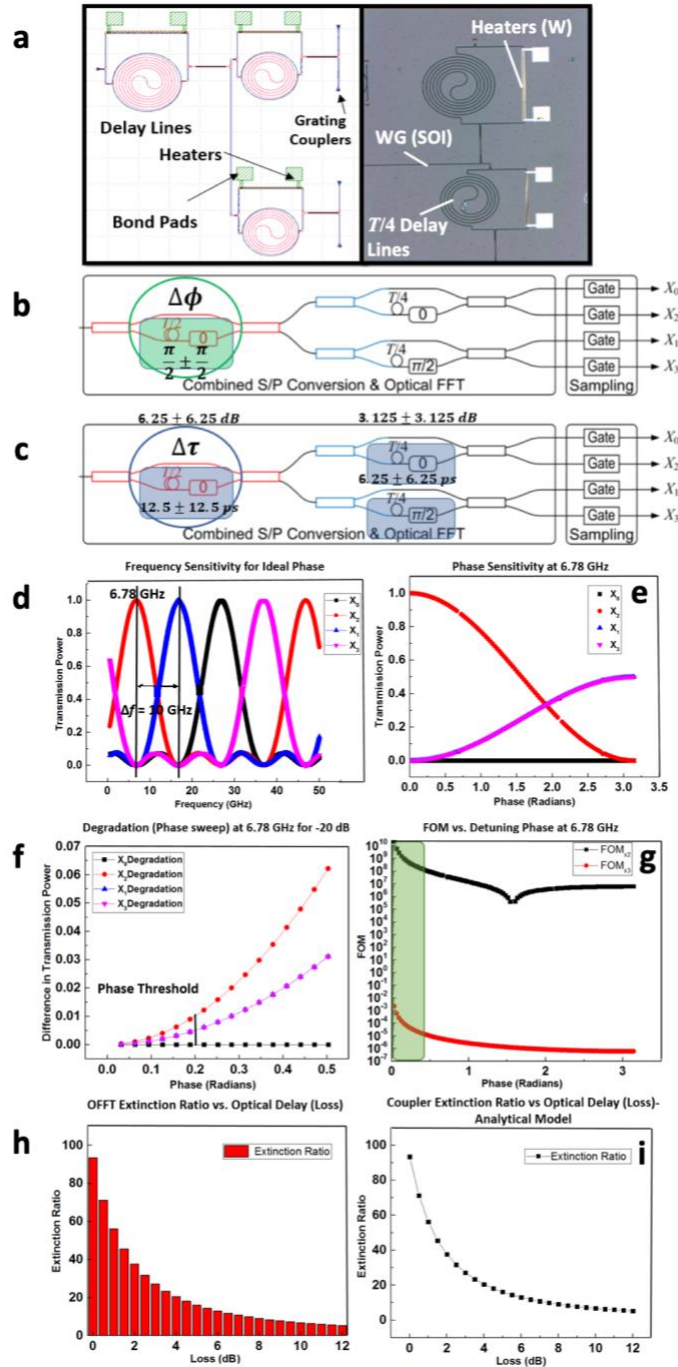


Figure 3. OFFT sensitivity analysis with respect to phase coherence and amplitude loss. **a**, An $N = 4$ OFFT in silicon photonics, layout (left) and microscope image (right), shows the area budget being dominated by spiral delay waveguide stages. Physical area of the optical delay required in the serial architecture limits the scaling performance of the OFFT to small N . Heater (width = $8 \mu\text{m}$) are used for coherence phase control. $\lambda_{\text{signal}} = 1550 \text{ nm}$, $n_{\text{WG-mode}} = 2.5$. Design fabricated in standard SOI (epi = 220 nm , BOX = $2 \mu\text{m}$). The length of the shorter arms of the MZI for the first stage is $500 \mu\text{m}$ and for the second stage is $440 \mu\text{m}$. **b**, Phase sensitivity analysis tests setup of the OFFT's first stage interferometer in terms of **c**, Time delay from $12.5 \pm 12.5 \text{ ps}$ ($T/4 \pm T/4$) ps with increments of 0.5 dB for the first stage Mach-Zehnder interferometer. **d**, Frequency Sensitivity Analysis on the transmission power (transfer function) of OFFT at ideal phase, **e**, Phase Sensitivity Analysis on the transmission power at probe frequency of 6.78 GHz . **f**, Degradation for -20 dB tolerance and **g**, FOM as a function of detuning phase at 6.78 GHz probe frequency- where X_2 has the ideal FOM while X_3 is minimal leakage from X_3 bin (similar to X_0 and X_1 , not shown). **h**, Extinction ratio of the OFFT full system as a function of physical optical loss from the spiral waveguides (delay lines), **i**, Analytical exponential fit based on an ideal coupler.

Figure 4

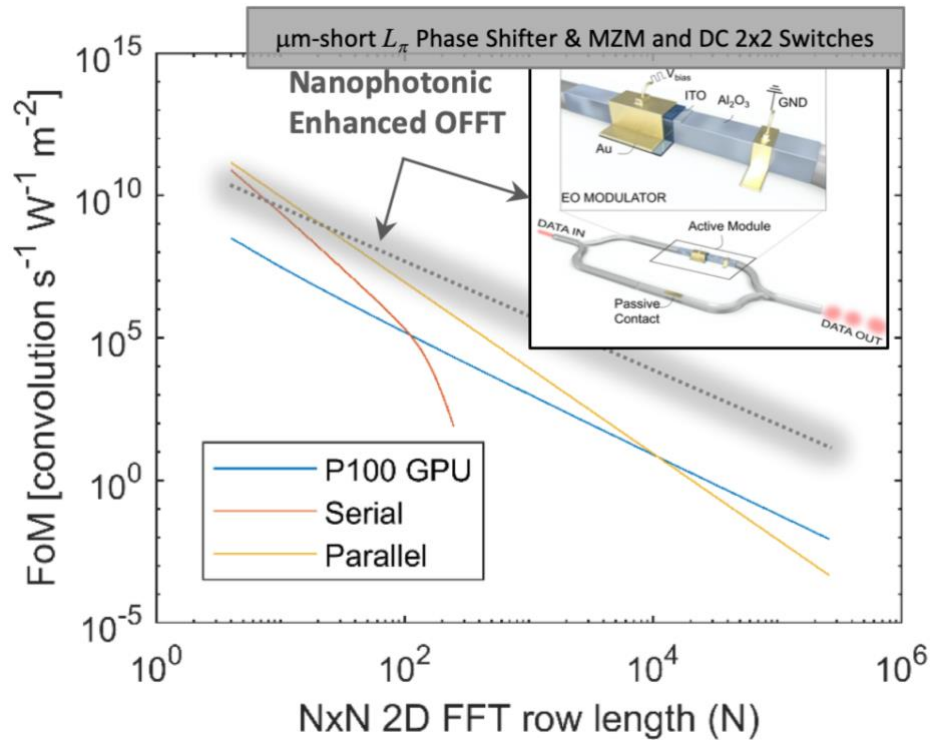


Figure 4. Power-Area-Speed performance analysis of the core of the CNN engine based on OFFT. A model of the figure of merit, Convolutions $s^{-1} W^{-1} m^{-2}$, vs N shows the OFFT architecture outperforming the NVIDIA P100 in for $N < 10^2$ in a serial configuration and less than $N < 10^4$ in parallel configurations. Details are: FLOPS per convolution: $20N^2 \log_2(N) + N^2$. ADC(DAC): 56(100) GSa/s @ 2(2.5)W power dissipation; optical component losses: 1st spiral = 0.7 dB; 2x2 directional coupler loss = 1.0 dB; y-splitter and combiners = 3.0dB; grating coupler (freespace-to-chip) = 4.0 dB; electro-optic modulator = 3.5dB. Inset: nanophotonic device enhancements enable micrometer-short optoelectronic devices such as i) π -phase shifters leading to compact MZI modulators [25,26,28] or electro-absorption modulators [27], and also to $<10 \mu m$ -short 2x2 directional couplers [30] allowing for better N -scaling of OFFT-based convolutions.

References

1. Norman P. Jouppi, et al. "In-Datcenter Performance Analysis of a Tensor Processing Unit" *Comput. Archit. News* 45, 2, 1–12 (2017).
2. Goodman, J. W. Introduction to Fourier Optics, Roberts & Company (2005).
3. X. Lin, Y. Rivenson, N. T. Yardimci, M. Veli, Y. Luo, M. Jarrahi, A. Ozcan, "All-optical machine learning using diffractive deep neural networks" *Science* 361, 1004–1008 (2018).
4. V. J. Sorger, et al. "Photonic Convolutional Processor of for Network Edge Computing" *ONR Electronic Warfare*, (accessed Jan-2020).
5. Z. Hu, M. Miscuglio, J. George, Y. Alkabani, T. Gazhawi, and V. Sorger, "Highly-parallel Optical Fourier Intensity Convolution Filter For Image Classification," FIO, paper JW4A.101 (2019).
6. A. N. Tait, M. A. Nahmias, B. J. Shastri, and P. R. Prucnal, "Broadcast and weight: an integrated network for scalable photonic spike processing" *Journal of Lightwave Technology*, 32, 21, pp. 3427–3439 (2014).
7. A. N. Tait, A. X. Wu, T. F. de Lima, E. Zhou, B. J. Shastri, M. A. Nahmias, and P. R. Prucnal, "Microring weight banks" *IEEE Journal of Selected Topics in Quantum Electronics* 22, 6, pp. 312–325 (2016).
8. Y. Shen, N. C. Harris, S. Skirlo, M. Prabhu, T. Baehr-Jones, M. Hochberg, X. Sun, S. Zhao, H. Larochelle, D. Englund et al., "Deep learning with coherent nanophotonic circuits" *Nature Photonics*, vol. 11, no. 7, p. 441 (2017).
9. R. Amin, J. George, S. Sun, T. Ferreira de Lima, A. N. Tait, J. Khurgin, M. Miscuglio, B. J. Shastri, P. R. Prucnal, T. El-Ghazawi, V. J. Sorger "ITO-based Electro-absorption Modulator for Photonic Neural Activation Function" *APL Materials* 7, 081112 (2019).
10. M. Miscuglio, G.C. Adam, D. Kuzum, V.J. Sorger "Roadmap on Material-Function Mapping for Photonic-Electronic Hybrid Neural Networks" *APL Materials* 7, 100903 (2019).
11. A. Mehrabian, M. Miscuglio, Y. Alkabani, V. J. Sorger, T. El-Ghazawi "A Winograd-based Integrated Photonics Accelerator for Convolutional Neural Networks" *IEEE J. of Selected Topics in Quantum Electronics* 26(1), 1-12 (2019).
12. M. Miscuglio, A. Mehrabian, Z. Hu, S.I. Azzam, J.K. George, A.V. Kildishev, M. Pelton, V.J. Sorger "All-optical Nonlinear Activation Function for Photonic Neural Networks" *Optical Material Express* 8(12), 3851-3863 (2018).
13. T. W. Hughes, M. Minkov, Y. Shi, S. Fan "Training of photonic neural networks through in situ backpropagation and gradient measurement" *Optica* 5, 7 pp. 864-871 (2018).
14. S. Colburn, Y. Chu, E. Shlizerman, A. Majumdar "An Optical Frontend for a Convolutional Neural Network" *Applied Optics*, Vol. 58, Issue 12, pp. 3179-3186 (2019).
15. e.g. Pluto Holoeye, (<https://holoeye.com/spatial-light-modulators/>), online (accessed Jan-2020).
16. M. E. Marhic. "Discrete fourier transforms by single-mode star networks," *Opt. Lett*, vol. 12, pp. 63-65, 1987.
17. D. Hillerkuss et al., "Novel optical fast fourier transform scheme enabling real-time OFDM processing at 392 Gbit/s and beyond," 2010 Conference on Optical Fiber Communication (OFC/NFOEC), collocated National Fiber Optic Engineers Conference, San Diego, CA, pp. 1-3 (2010).
18. Z. Wang *et al.*, "Optical FFT/IFFT circuit realization using arrayed waveguide gratings and the applications in all-optical OFDM system." *Optics Express*, vol. 19, no. 5, pp. 4501, 2011.
19. D. Hillerkuss *et al.*, "26 tbit s-1 line-rate super-channel transmission utilizing all-optical fast fourier transform processing," *Nature Photonics*, vol. 55, no. 6, pp. 364-371, 2011.
20. A. Krizhevsky, I. Sutskever, and G. E. Hinton, "ImageNet classification with deep convolutional neural networks," *Advances in Neural Information Processing Systems* vol. 25, F. Pereira et al, Ed. Curran Associates, Inc, pp. 1097-1105 (2012).
21. R. Gray and J. Goodman, Fourier Transforms an Introduction for Engineers, Springer Science & Business Media, 1995, pp. 74-78.
22. Chrostowski, L., Hochberg, M. Silicon Photonics Design: From Devices to Systems, Cambridge University Press (2015).
23. Y. Gui, M. Miscuglio, Z. Ma, M. T. Tahersima, V. J. Sorger "Towards integrated metatronics: a holistic approach on precise optical and electrical properties of Indium Tin Oxide" *Nature Scientific Reports* 9(1), 1-10 (2019).
24. N. Kinsey, J. Khurgin "Nonlinear epsilon-near-zero materials explained" *Opt. Mat. Exp.* 9, 7, 2793-2796

(2019).

25. R. Amin, R. Maiti, C. Carfano, Z. Ma, M.H. Tahersima, Y. Lilach, D. Ratnayake, H. Dalir, V.J. Sorger “0.52 V-mm ITO-based Mach-Zehnder Modulator in Silicon Photonics” *APL Photonics* 3,12 (2018).
26. R. Amin, R. Maiti, J. K. George, X. Ma, Z. Ma, H. Dalir, M. Miscuglio, V. J. Sorger “A lateral MOS-Capacitor Enabled ITO Mach- Zehnder Modulator for Beam Steering” *Journal Lightwave Technology* doi: 10.1109/JLT.2019.2956719 (2019).
27. M. H. Tahersima, Z. Ma, Y. Gui, S. Sun, H. Wang, R. Amin, H. Dalir, R. Chen, M. Miscuglio, V. J. Sorger, “Coupling-enhanced Dual ITO Layer Electro-absorption Modulator in Silicon Photonics”, *Nanophotonics* 8, 9, (2019).
28. R. Amin, R. Maiti, Y. Gui, C. Suer, M. Miscuglio, E. Heidari, R. T. Chen, H. Dalir, V. J. Sorger “Broadband Sub- λ GHz ITO Plasmonic Mach-Zehnder Modulator on Silicon Photonics” *arXiv* preprint: submit/2989492 (2020).
29. Hillerkuss, D. et al., Simple all-optical FFT scheme enabling Tbit/s real-time signal processing, *Opt. Express* 18, 9324-9340 (2010).
30. C. Ye, K. Liu, R. Soref, V. J. Sorger, “A compact plasmonic MOS-based 2x2 Switch” *Nanophotonics*, 4, 1, pp. 261-268 (2015).
31. J. Meng, M. Miscuglio, J. K. George, et al. “Electronic Bottleneck Suppression in Next-generation Networks with Integrated Photonic Digital-to-analog Converters” Nature Communications, under review (2019). *arXiv* preprint: 1911:02511. (2019).
32. NVIDIA. *NVIDIA TESLA P100 GPU Accelerator* [Online]. Available: <https://images.nvidia.com/content/tesla/pdf/nvidia-tesla-p100-PCIe-datasheet.pdf>. (accessed Jan-2020).
33. H. Huang *et al.*, "An 8-bit 100-GS/s distributed DAC in 28-nm CMOS for optical communications," *IEEE Trans. Microw. Theory Tech*, vol. 63, no. 4, pp. 1211-1218, 2015.
34. Fujitsu.(2010). *56GSa/s 8-bit Analog-to-Digital Converter* [Online]. Available: http://www.fujitsu.com/downloads/MICRO/fma/pdf/56G_ADC_FactSheet.pdf.
35. Y. Zhang *et al.*, "A high-responsivity photodetector absent metal-germanium direct contact," *Optics Express*, vol. 22, no. 9, pp. 11367, 2014.
36. D. A. B. Miller. "Attojoule optoelectronics for low-energy information processing and communications," *J. Lightwave Tech.*, vol. 35, no. 3, pp. 346-396, 2017.
37. J. K. George, A. Mehrabian, R. Armin, J. Meng, T. Ferreira De Lima, A. N. Tait, B. Shastri, P. Prucnal, T. El-Ghazawi, V. J. Sorger “Noise and Nonlinearity of Electro-optic Activation Functions in Neuromorphic Compute Systems” *Optics Express* 27, 4 (2019).
38. J. Meng, M. Miscuglio, J. K. George, V. J. Sorger “Electronic Bottleneck Suppression in Next-generation Networks with Integrated Photonic Digital-to-analog Converters” Nature Communications, under review (2019). *arXiv* preprint: 1911:02511.
39. Narayana, V. K. et al. “MorphoNoC: Exploring the Design Space of a Configurable Hybrid NoC using Nanophotonics” *Microprocessors and Microsystems*, doi.org/10.1016/j.micpro.2017.03.006. (2017).